Geophysical Journal International

Geophys. J. Int. (2017) **209,** 876–889
Advance Access publication 2017 February 17
GJI Seismology

doi: 10.1093/gji/ggx064

Hydrostratigraphy characterization of the Floridan aquifer system using ambient seismic noise

Stephanie R. James, Elizabeth J. Screaton, Raymond M. Russo, Mark P. Panning, Paul M. Bremner, A. Christian Stanciu,* Megan E. Torpey, Sutatcha Hongsresawat† and Matthew E. Farrell

Department of Geological Sciences, University of Florida, Gainesville, FL, USA. E-mail: srjames88@ufl.edu

Accepted 2017 February 15. Received 2017 February 10; in original form 2016 August 30

SUMMARY

We investigated a new technique for aquifer characterization that uses cross-correlation of ambient seismic noise to determine seismic velocity structure of the Floridan aquifer system (FAS). Accurate characterization of aquifer systems is vital to hydrogeological research and groundwater management but is difficult due to limited subsurface data and heterogeneity. Previous research on the carbonate FAS found that confining units and high permeability flow zones have distinct seismic velocities. We deployed an array of 9 short period seismometers from 11/2013 to 3/2014 in Indian Lake State Forest near Ocala, Florida, to image the hydrostratigraphy of the aquifer system using ambient seismic noise. We find that interstation distance strongly influences the upper and lower frequency limits of the data set. Seismic waves propagating within 1.5 and 7 wavelengths between stations were optimal for reliable group velocity measurements and both an upper and lower wavelength threshold was used. A minimum of 100–250 hr of signal was needed to maximize signal-to-noise ratio and to allow cross-correlation convergence. We averaged measurements of group velocity between station pairs at each frequency band to create a network average dispersion curve. A family of 1-D shear-wave velocity profiles that best represents the network average dispersion was then generated using a Markov Chain Monte Carlo (MCMC) algorithm. The MCMC algorithm was implemented with either a fixed number of layers, or as transdimensional in which the number of layers was a free parameter. Results from both algorithms require a prominent velocity increase at ∼200 m depth. A shallower velocity increase at ∼60 m depth was also observed, but only in model ensembles created by collecting models with the lowest overall misfit to the observed data. A final round of modelling with additional prior constraints based on initial results and well logs produced a mean shear-wave velocity profile taken as the preferred solution for the study site. The velocity increases at ∼200 and ∼60 m depth are consistent with the top surfaces of two semi-confining units of the study area and the depths of high-resistivity dolomite units seen in geophysical logs and cores from the study site. Our results suggest that correlation of ambient seismic noise holds promise for hydrogeological investigations. However, complexities in the cross-correlations at high frequencies and short traveltimes at low frequencies added uncertainty to the data set.

Key words: Probability distributions; Hydrogeophysics; Surface waves and free oscillations; Seismic interferometry; Seismic noise.

1 INTRODUCTION

Cross-correlation of ambient noise has been widely used to determine crustal seismic velocity structure (Campillo & Paul 2003; Shapiro & Campillo 2004; Yao *et al*. 2006; Moschetti *et al*. 2007; Yang *et al*. 2007; Lin *et al*. 2008; Gallego *et al*. 2010; Bremner *et al*., in preparation). Ambient noise sources produce seismic surface waves that propagate within the earth's crust. Heterogeneities

*Now at: Department of Earth Sciences, University of Oregon, Eugene, OR, USA.
†Now at: Geoscience Division, School of Interdisciplinary Studies, Mahidol University-Kanchanaburi Campus, Kanchanaburi, Thailand.

© The Authors 2017. Published by Oxford University Press on behalf of The Royal Astronomical Society.

within the earth scatter these waves. In theory, the wide distribution of noise sources combined with this scattering effect produce a random, diffusive wavefield that operates continuously through time (Sabra *et al*. 2005). Records of waves that travel between two seismic stations can be cross-correlated to extract the impulse response (or empirical Green's function, EGF) of the subsurface between those stations: in effect, the first station becomes a virtual source for the seismic wave recorded at the second (Shapiro & Campillo 2004; Shapiro *et al*. 2005). The cross-correlation function of vertical component records is interpreted as primarily the result of fundamental mode Rayleigh wave energy, although other energy, such as body waves and higher modes, may also be present. In a heterogeneous media, Rayleigh wave energy is dispersive, meaning that velocity differences between waves of differing frequencies provide constraints on velocity variations with depth (Campillo & Paul 2003).

The retrieval of EGFs from ambient noise is an efficient technique that can sample 3-D Earth structure in the absence of earthquake activity or an active source. This method has been successfully applied to surface waves within the microseismic frequency band (0.05–0.2 Hz) of strong signals produced by ocean waves (Bensen *et al*. 2007; Lin *et al*. 2013; Ojo *et al*. 2017). Correlation of high frequency (>1 Hz) ambient noise has been used to study earth structure in the upper kilometre (Lin *et al*. 2013; Mordret *et al*. 2013; Pan *et al*. 2016), the shallow subsurface for geotechnical purposes down to tens of metres (Halliday *et al*. 2008; Picozzi *et al*. 2009; Shirzad *et al*. 2015), and in monitoring applications (Sens-Schönfelder & Wegler 2006; Brenguier *et al*. 2011; Mainsant *et al*. 2012; Gassenmeier *et al*. 2015; Chaves & Schwartz 2016). High frequency seismic noise is produced by anthropogenic activities such as vehicle traffic as well as natural sources such as wind and ocean waves (Halliday *et al*. 2008; Picozzi *et al*. 2009; Zhang *et al*. 2009).

We examined whether high frequency ambient noise can be used to image hydrostratigraphy of the upper several hundred metres of a carbonate aquifer system. Low permeability confining units within the Floridan aquifer system (FAS) were chosen as the primary target of this pilot study. In general, the dense and rigid framework of low permeability confining unit material exhibits faster seismic velocities relative to zones of high permeability. This relationship has been recorded in prior studies using sonic logs in south Florida (Maliva & Walker 1998; MWH Americas Inc. 2004). Due to scarcity of deep boreholes and the heterogeneity of karst aquifers, the continuity of confining units is uncertain. Correlation of ambient seismic noise could provide a useful new technique for addressing this problem, particularly in areas where costly, closely spaced borings or active source methods are impractical or undesirable. In this study, we demonstrate and evaluate the utility of ambient noise for hydrogeological investigations, particularly in areas with limited prior information.

We used a Bayesian inference approach to invert group velocity measurements from cross-correlations of ambient seismic noise to determine 1-D vertical seismic velocity profiles. The level of uncertainty and limited prior information in this study made this inversion scheme advantageous since Bayesian inference quantifies the posterior probability distribution based on the observed data with few prior constraints. Resulting profiles were compared to the known hydrogeological framework, as well as to electrical resistivity logs from the study site. We also investigated the dependence of modelling results on whether the number of structural layers in the 1-D velocity profiles was a fixed or a free parameter, as well as the ensemble collection method. In addition, we address questions pertaining to the deployment logistics to inform future array configurations and deployment duration.

2 BACKGROUND: THE FAS

The FAS consists of a thick sequence of Cenozoic carbonate units overlain by siliciclastic deposits. The degree of dolomitization and occurrence of evaporite layers within the FAS generally increases with depth (Miller 1986). The base of the FAS is defined as the first occurrence of a massively bedded anhydrite layer within the Cedar Keys Formation (Miller 1986; Tibbals 1990; Williams & Kuniansky 2015). The FAS can be subdivided into an Upper Floridan aquifer system (UFAS) and Lower Floridan aquifer system (LFAS), separated by one or more lower permeability confining or semi-confining units (Miller 1986; Copeland *et al*. 2009; Williams & Kuniansky 2015). The UFAS is a confined aquifer except where the overlying low permeability siliciclastic layers within the Hawthorn Group have been removed by erosion.

Differences in depositional conditions and diagenetic alteration processes, such as degrees of cementation, dissolution, dolomitization and recrystallization result in complex heterogeneity of the FAS. The diagenetic processes also form unique rock fabrics which alter the elastic properties of the rock. The associated velocity patterns do not simply reflect compositional variations but are instead largely controlled by the amount and type of porosity present. Zones of microcrystalline dolomite and fine grained limestone have been shown to yield faster seismic velocities compared to more porous sucrosic dolomite and coarse grained limestone (Anselmetti & Eberli 1993). Rayleigh wave velocity is primarily a function of shear-wave velocity (Shapiro *et al*. 2005). Laboratory and borehole measurements show compressional-wave velocities range from 1 to 6.77 km s^{-1} and shear-wave velocities range between 0.75 and 3.4 km s^{-1} (Anselmetti & Eberli 1993; MWH 2004; Kazatchenko *et al*. 2006; Parra *et al*. 2006, 2009). The wide range of seismic velocities reflects the extreme variability in physical properties of diagenetically altered carbonate rock, and represents hydrogeologically relevant variation in porosity and permeability.

2.1 Study area

Our study was conducted within Indian Lake State Forest, near Ocala, Florida (Fig. 1). The state forest is located within the Ocklawaha River surface water drainage basin and the Silver Springs springshed of the UFAS (Tibbals 1990). Through collaboration with the St. Johns River Water Management District, the site was selected based largely on accessibility, availability of well data, and its importance as a recharge zone for the Silver Springs group. In central Marion County, Florida, the UFAS is the primary source of municipal water; however, recent increases in water demand have motivated research into exploring the LFAS as an additional water resource. Therefore, understanding the extent, thickness and number of confining units at the study site can help determine the hydraulic connection between the upper and lower aquifer and consequently the viability of the LFAS as an alternative water source.

The base of the FAS is approximately 610 m below ground surface (mbgs) in central Florida and the FAS consists of the Ocala limestone, Avon Park Formation, Oldsmar Formation and the Cedar Keys Formation (Fig. 2; Miller 1986; Tibbals 1990; Williams & Kuniansky 2015). Within central and western Marion County, Florida, the Ocala limestone occurs at or near land surface. Scattered

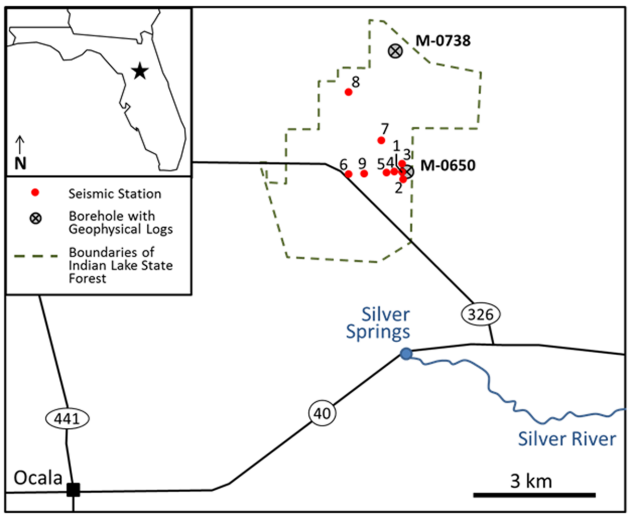

Figure 1. The study region is within Indian Lake State Forest which lies approximately 8 km northeast of Ocala, Florida and ~2 km north of Silver Springs. The locations of the nine seismic stations within the study site (red circles) along with the two deep boreholes with geophysical logging information (M-0650 and M-0738 – crossed grey circles) are shown.

remnants of the Hawthorn group and thin (<10 m) units of unconsolidated sands, silts and clays cover the Ocala limestone in places. Lithologic information, caliper logs, natural gamma ray logs and electrical resistivity logs are available from two deep (>300 m) borings, M-0650 and M-0738, within the study site (Fig. 3). Electrical resistivity logs in particular can be useful when compared to seismic velocity profiles as both are dependent on formation porosity. Based on information from M-0650, the top of the Ocala limestone is at 6 mbgs. Two lower permeability units (labelled either middle confining units or semi-confining units) have been recognized from ~60 to 125 mbgs and ~200 to 270 mbgs (Miller 1986; Williams & Kuniansky 2015).

3 METHODS

3.1 Field acquisition

Nine short-period Sercel L-22 seismometers (on loan from the Incorporated Research Institutions for Seismology (IRIS) Portable Array Seismic Studies of the Continental Lithosphere (PASSCAL) Instrument Center in Socorro, New Mexico) were deployed in Indian Lake State Forest for 17 weeks. Five seismic stations were installed on 2013 November 5 and the remaining four were installed on 2013 November 7. Station maintenance and data downloading occurred on 2013 December 23 and 2014 January 21. On 2014 March 9 all nine stations were removed from the study site.

The sensors have a corner frequency of 2 Hz (Fig. S1). Ground motion was recorded on three channels at a sampling rate of 100 samples per second. The seismic array was configured such that the majority of the stations were organized in an east–west line but also ensured that some stations were located near the two boreholes on the site. In particular, stations 1–5 were arranged at close interstation spacing near the M-0650 borehole (Fig. 1). The stations were spaced at varying distances between 0.18 and 2.6 km. This array design was expected to limit data quality for inversion, but was needed to test the relationship between interstation distances and coherent frequencies.

3.2 Data processing

Hour-long records for the vertical component, 100 samples per second data stream, were pre-processed by removing the mean, trend, and instrument response. The instrument response was removed using poles and zeros for the sensor type provided by IRIS-PASSCAL. We used the method described in Bensen *et al*. (2007) to calculate the cross-correlations. To remove the possibility of bias toward large amplitude events, such as earthquakes and other high energy events from passing vehicles, temporal normalization was done by converting each record into one-bit signals. The frequency spectrum was then flattened through spectral whitening. Cross-correlations for each station pair were conducted for each hour-long record and the results were stacked.

Theoretical studies of ambient seismic noise have shown that the empirical Green's function of the subsurface between stations A and B (G_{AB}), and the reverse (G_{BA}), can be estimated from the time derivative of the cross-correlation of the diffuse noise records of those stations (C_{AB} and C_{BA}) (Lobkis & Weaver 2001; Lin *et al*. 2008). Taking the time-derivative is more relevant for phase velocity studies since it causes a $\pi/2$ phase shift but does not impact the cross-correlation waveform and associated group velocity (Roux *et al*. 2005; Sabra *et al*. 2005). There is also a risk of introducing high frequency noise when using the derivative (Sabra *et al*. 2005), but we found no significant impact so kept the time-derivative calculation in our procedure for completeness. The stacked cross-correlated signals for each station pair were generally asymmetric. We made them symmetric by averaging the positive (causal) and negative (acausal) time lag directions (Lin *et al*. 2008; Gallego *et al*. 2010; Bremner *et al*., in preparation):

$$G_{AB}\ (t) = G_{BA}\ \ (t) = -\frac{\mathrm{d}}{\mathrm{d}t}\left[\frac{C_{AB}\,(t) + \ C_{BA}\,(t)}{2}\right] \quad 0 \le t < \infty. \quad (1)$$

These symmetric EGFs were multiplied by a step function (Heaviside) to reduce the acausal branch to zero amplitude, which would otherwise influence the causal signals by smearing from filtering. The resulting one-sided correlation records were bandpass filtered using a Butterworth filter (2 poles, 2 passes) at a total of 13 frequency bands between 1 and 9 Hz. The width of each frequency band was selected as a compromise due to the trade-off between resolution in time and resolution in frequency. Each corner frequency is plus or minus 10 per cent of the centre frequency for that band, forcing the band widths to be scaled by frequency. Each band overlaps with adjacent bands to ensure full depth coverage. Group velocity measurements for each station pair were made by measuring the traveltime at the peak of the envelope of the coherent signal at each frequency band.

3.3 Markov Chain Monte Carlo (MCMC) modelling

Group velocity measurements at each frequency band were subjected to quality control checks. The signal-to-noise ratio (SNR) of each cross-correlation was calculated based on the rms amplitude of the signal window compared to the rms amplitude of a noise window. Measurements with SNR values below 6 were omitted. Estimated wavelengths for each frequency were calculated and compared to the interstation distances of each station pair. We omitted group velocity measurements for frequency bands whenever interstation distances were less than 1.5 wavelengths or greater than 7 wavelengths of the particular frequency. The lower cut-off is a quality control step commonly used in ambient noise studies to satisfy the far-field approximation (Bensen *et al*. 2008; Lin *et al*. 2008; Tsai 2009). The

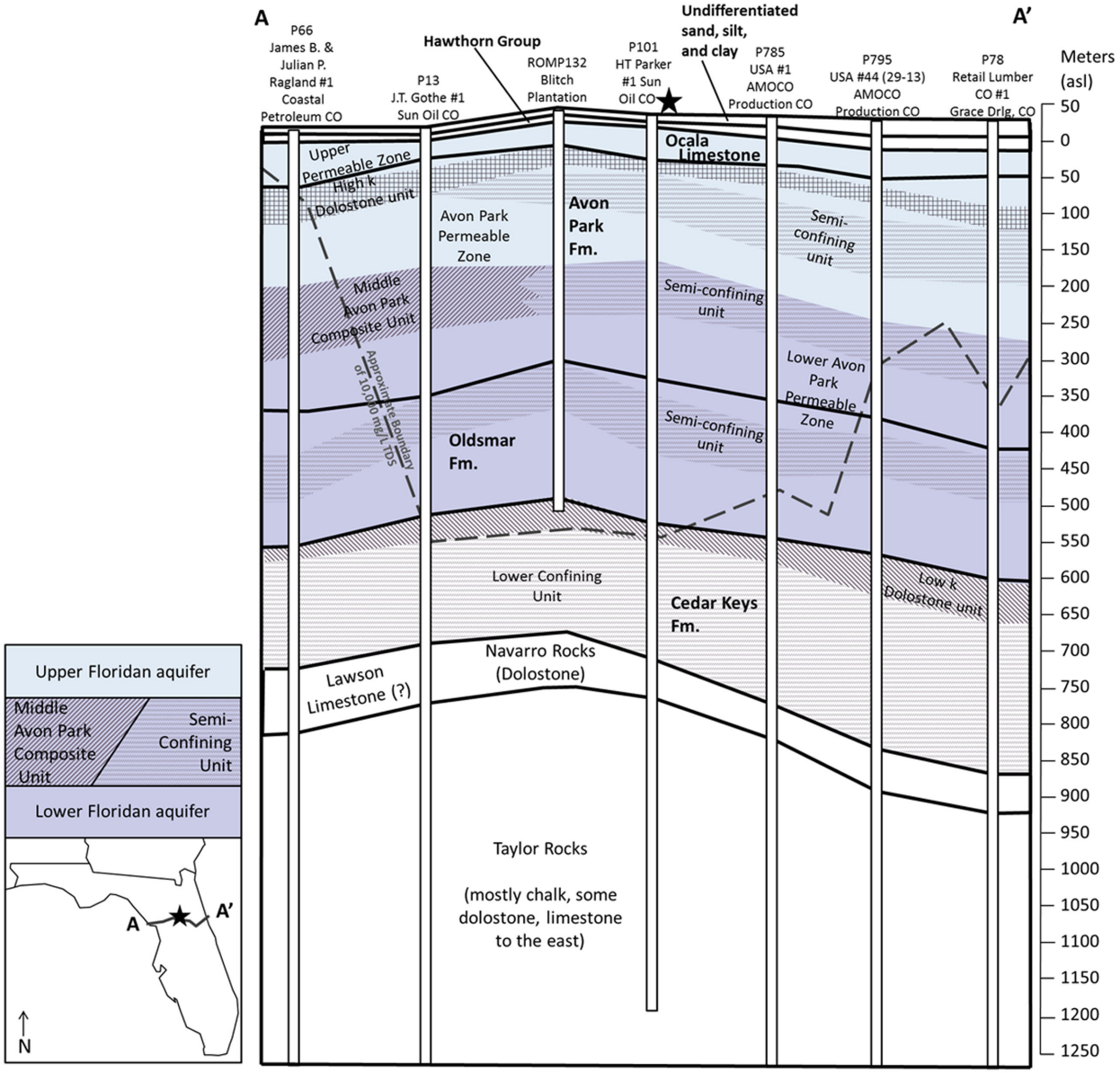

Figure 2. Generalized hydrogeological cross-section through the study area (black star). Adapted from Plate 20 of Williams & Kuniansky (2015).

upper cut-off of seven wavelengths was added with the assumption that strong attenuation of higher frequency waves travelling longer distances can degrade the signal (Shapiro & Campillo 2004; Campillo 2006; Lawrence *et al*. 2013; discussed further in Results). Shear-wave velocity bounds of 0.1–3 km s^{-1} were enforced such that any measurements outside that range were considered unreliable and omitted. The realistic bounds on shear-wave velocity were shifted toward slightly slower velocities compared to data available from studies in south Florida in order to reflect the different setting of the study site (i.e. higher degree of dissolution, shallower depths). Due to these checks on quality, many measurements were eliminated and the dispersion curves for individual station pairs were incomplete. Therefore, we averaged all remaining measurements at each frequency band to create a network average dispersion curve.

We applied a MCMC scheme to the network average group velocity measurements in order to generate a family of 1-D shear velocity models that best fits the data. Two forms of the MCMC algorithm were applied. The first used a fixed number of layers (k) and the second was transdimensional, meaning that k was a free parameter (Bodin & Sambridge 2009; Bodin *et al*. 2012a,b). The transdimensional form of the algorithm was developed to test the degree of uncertainty in our results and to eliminate the dependence of model structure on a fixed number of layers imposed *ad hoc*. In both cases the total model depth was fixed, and a lower half-space of constant velocity was included as another free parameter. The interface depth between layers and the shear-wave velocity of each layer were free parameters in both versions of the algorithm (Fig. 4). The initial model parameters for each chain were drawn from the prior distribution of each parameter (Table S1). The algorithm then proceeded iteratively. Only one model parameter was perturbed in each iteration to generate a new model and to explore the distribution of models that adequately fit the observed data. We used the program *surf96* from Computer Programs in Seismology (Herrmann & Ammon 2002) to solve the forward problem to generate dispersion curves based on the newly created model. The predicted group velocity dispersion, $\mathbf{d}_{\mathbf{pre}}$, from *surf96* was then

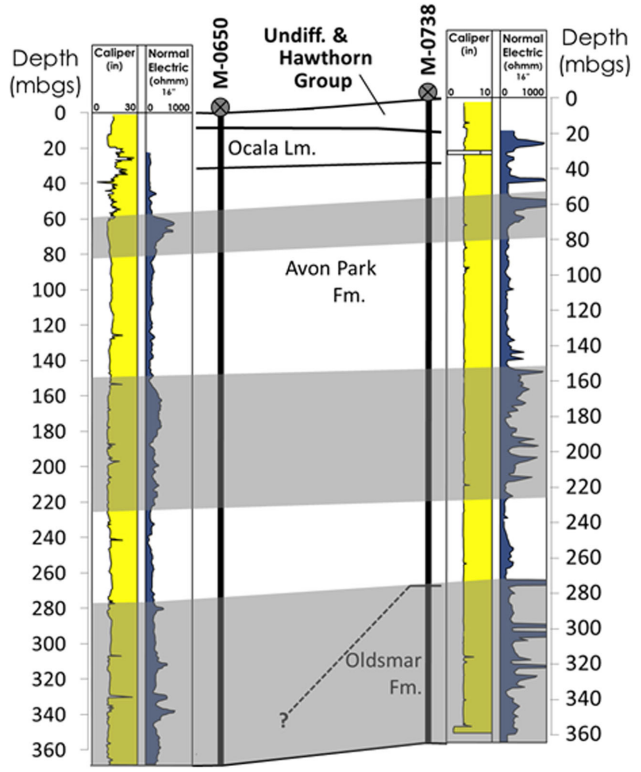

Figure 3. Geological cross-section between the M-0650 and M-0738 boreholes within Indian Lake State Forest. Caliper (yellow) and electrical resistivity (dark blue) logs for each borehole are shown. Continuous zones of high resistivity are shaded grey and connected between the two boreholes. The top of the shallowest high resistivity zone has previously been defined as the top of a semi-confining unit (MCU-1 of Miller 1986) (St. Johns River Water Management District, Hydrogeologic Information System).

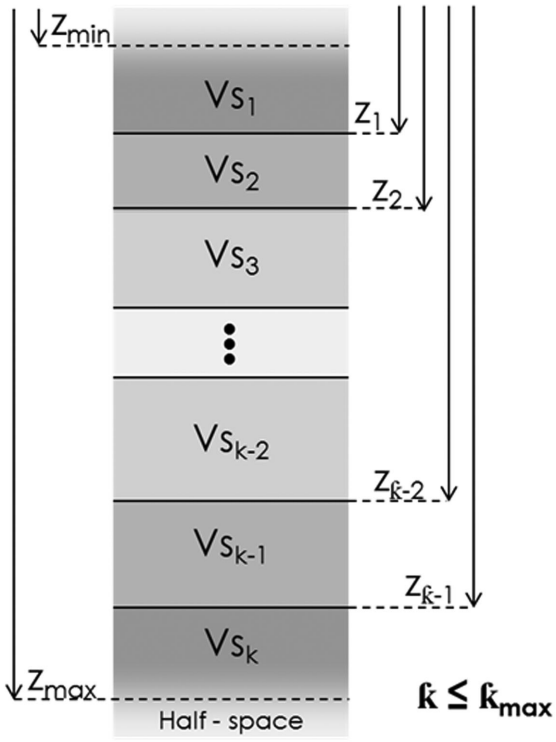

Figure 4. 1-D vertical shear-wave model parameterization with k layers. Each layer has a uniform shear-wave velocity (Vs). The interface depths between layers (z) are restricted between the user defined minimum and maximum depths, z_{min} and z_{max}, respectively. In the transdimensional approach, k is restricted between user defined k_{min} and k_{max}. The non-transdimensional approach uses a constant k. Adapted from Malinverno (2002).

compared to the measured dispersion curve, $\mathbf{d}_{obs}$. The misfit for each data point was calculated and weighted by one over the variance for that frequency band, $\boldsymbol{\sigma}_{\mathbf{d}}^2$. The overall error of the model, $\phi(\mathbf{m})$, was calculated as the sum of the squares for each weighted misfit. The acceptance criterion, $\alpha(\mathbf{m}'|\mathbf{m})$ is defined as:

$$\alpha(\boldsymbol{m}'|\boldsymbol{m}) = \min\left[1,\ \exp\left\{\frac{-\phi(\boldsymbol{m}') - \phi(\boldsymbol{m})}{2}\right\}\right] \tag{2}$$

$$\phi(\boldsymbol{m}) = \sum_{i}^{N}\left(\frac{d_i^{\text{pre}} - d_i^{\text{obs}}}{\sigma_i^d}\right)^2, \tag{3}$$

where $\mathbf{m}$ is the previous model, $\mathbf{m}'$ is the proposed model, $\mathbf{m}'|\mathbf{m}$ indicates $\mathbf{m}'$ conditional on $\mathbf{m}$, and min[a, b] is a function that returns the minimum of values a and b. The acceptance term was then compared to a random number, w, drawn from a uniform distribution between 0 and 1. If the acceptance term is less than w, then the model was rejected and the iteration repeated. Otherwise, the process advances to the next iteration. This step allows the chance for a model with a lower acceptance term, that is a poorer fit, to be retained which prohibits the search of the model space from becoming trapped within local minima. The posterior distribution of models approaches the conditional probability density function (PDF) given the observed data.

The fixed-k MCMC algorithm was run for 10 chains of 1000 iterations each. The models' total depth constraint and number of layers were fixed while the interface depths and shear wave velocity of each layer and the half-space were perturbed by a random amount drawn from a Gaussian distribution centred on the current value. We tested standard deviation values from 0.001–0.2 and monitored the model acceptance rate to select values that optimize the trade-off between exploration of the model space and computing time (Table S1). The variance values selected resulted in an average model acceptance rate of 55 per cent. An ensemble of retained models was created by taking the 500 models with the lowest error in each chain. The ensemble was then culled a final time to retain the best 1000 models from all chains. A variety of initial parameter combinations were imposed, spanning the total depth range of 200–600 m and two to five layers, to test the sensitivity of the modelling results to k and the total depth constraint.

The transdimensional version of the algorithm was implemented based on the method of Bodin *et al*. (2012a,b), with a slight modification in the calculation of the data covariance matrix, C_e, to include the standard deviations of the network average dispersion curve. In the Hierarchical Bayesian formulation, the hyperparameter, h, serves to scale the complexity of the model solutions to the uncertainty of the data. This eliminates the need to optimize the solution complexity manually by fixing the number of layers or adjusting the level of smoothing. Instead, the level of noise in the data determines the level of complexity required to fit the data (Bodin *et al*. 2012b). In other words, when data uncertainty is high a simple model is favoured. To implement the level of data noise as an unknown in the inversion, we defined the variance values in the diagonal of C_e as follows:

$$\boldsymbol{\sigma}_{\mathbf{T}}^2 = \sqrt{\boldsymbol{\sigma}_{\mathbf{d}}^2 + h^2}, \tag{4}$$

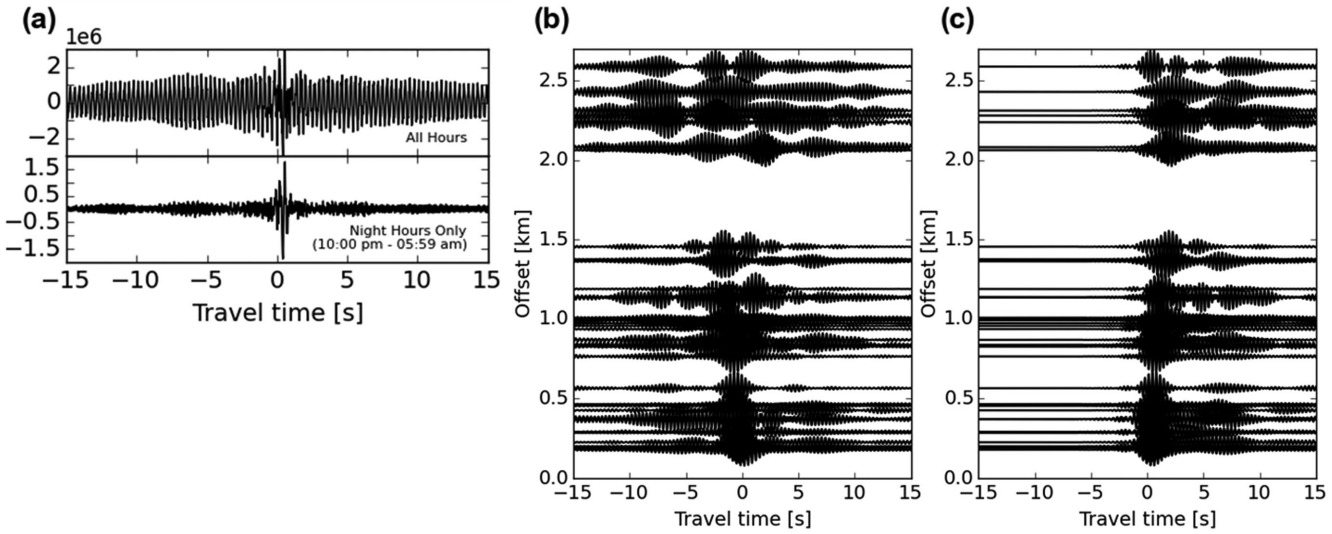

Figure 5. (a) Comparison of the cross-correlation for stations 6 and 9 for all hours of the data set and only night-time hours. (b) Record section for 3 Hz centre frequency. Cross-correlations are mostly asymmetric. (c) Cross-correlations were made symmetric by averaging the positive and negative time lags. Signals at positive time were isolated by multiplying cross-correlations by a step function to avoid smearing from negative time lags due to filtering.

where $\boldsymbol{\sigma}_{\mathbf{T}}^2$ is the total estimate of data uncertainty, and $\boldsymbol{\sigma}_{\mathbf{d}}^2$ is the vector of squared standard deviation values of the individual measurements at each frequency band. In the transdimensional case, model error is weighted by $\boldsymbol{\sigma}_{\mathbf{T}}$ instead of $\boldsymbol{\sigma}_{\mathbf{d}}$, as in the non-transdimensional case.

For the transdimensional scheme as adopted from Bodin *et al*. (2012a,b), each iteration begins by drawing a random integer between 1 and 5 to select the type of perturbation to be done. Thus, each change option has the same probability, $p = 1/5$: (1) *Change a velocity value*. Randomly select a layer, reassign its velocity according to a Gaussian probability distribution $q(v_i'|v_i)$ centred at the current value v_i and with user defined variance θ_1^2. (2) *Change an interface depth*. Randomly select an interface, perturb its depth according to a Gaussian probability distribution $q(z_i'|z_i)$ centred at the current depth z_i and with user defined variance θ_2^2. (3) *Birth*. Add a new layer by creating a new interface at a depth randomly selected from the prior distribution of interface depths. The velocity of the new layer was then assigned from a Gaussian proposal probability centred on the velocity of the layer in which the interface was added, with user defined variance θ_3^2. (4) *Death*. Delete an interface at random, in effect removing the layer above the chosen interface. (5) *Change the hyperparameter*. Perturb the current hyper-parameter value according to a Gaussian probability distribution $q(h'|h)$ centred at the current value h and with user defined variance θ_h^2.

In the transdimensional MCMC algorithm, the acceptance criterion for a model is not strictly dependent on the model error, as in eq. (2), but is calculated differently depending on the type of change proposed (Bodin *et al*. 2012a, appendix C). Therefore, the method of selecting models for the ensemble based on their error was no longer suitable. Instead, models from initial iterations were designated as part of the 'burn-in' period, after which the posterior probability distribution is assumed to be suitably represented and every Mth model is added to the ensemble. The increment M was chosen as a balance between maximizing sampling of the posterior distribution while excluding dependent samples. The number of iterations was increased to sample the posterior distribution more thoroughly. To optimize the trade-off between thoroughness of sampling and computing time, the number of iterations was tested by running the algorithm for 1000, 5000, 10 000, 20 000 and 50 000 iterations for each chain. The ensemble PDF was found to converge after 10 000 iterations, beyond which additional iterations filled in the PDF, smoothing the function but the form of the underlying structure was unchanged. In the interest of computing time, 10 000 iterations, was chosen. The first 5000 models were discarded as burn-in period, after which every 5th model was added to the ensemble. Verification tests were run to assess the accuracy of the algorithm (the Appendix).

4 RESULTS

4.1 Data quality and deployment logistics

Initial cross-correlations were obscured by a non-localized ∼3 Hz signal from an unknown source. Correlation of only night-time hours, between 10 pm and 6 am (local time), effectively minimized this dominant signal from a daytime source (Fig. 5a). The remainder of processing used only the 10 pm to 6 am data. The asymmetric cross-correlations were causal when the master station was to the west and/or south (Fig. 1); therefore, the noise wave-field propagated mostly from the southwest to the northeast. This finding is consistent with the location of the study site in relation to the city of Ocala, FL; given the likelihood that anthropogenic activity was the main source of noise in the frequency range of interest to this study. Averaging the causal and acausal branches of the cross-correlations and isolating the causal side improved signal clarity and identification, particularly when plotted in a record section (Figs 5b and c).

Frequencies were recorded in the range of 0.1–40 Hz. Cross-correlations filtered at frequencies lower than ∼1 Hz were centred at zero and resulted in spurious velocities—either negative or much greater than 3 km s^{-1}. At higher frequencies (>5 Hz), correlations included multiple signals, either due to shallow complex scattering or increased noise due to higher attenuation at high frequencies. The frequency bands nearest 2 Hz, the corner frequency of the sensors, resulted in clearly observed single arrivals that produced velocity estimates within the expected bounds. The lower and upper frequency limits of usable data were selected at 1 and 9 Hz,

respectively, based on the complications encountered with multiple signal arrivals at high frequencies and zero-centred arrivals at low frequencies.

The SNR of the cross-correlations was inversely related to station distances and frequency (Fig. S2). Station pairs separated by less than 0.5 km resulted in the highest SNR values. The inverse trend for frequency versus SNR was weaker than the distance relationship. Overall, the shortest interstation distances and lowest frequencies exhibited the highest SNR values. During the quality control steps in the processing, 91 per cent of measurements for short interstation distances and low frequencies (<2 Hz) were discarded either because they yielded unrealistically high velocities or the interstation distance was less than a minimum of 1.5 wavelengths of propagation. To test the necessity of this wavelength cut-off, wavelengths were calculated for each frequency band, using the measured network average velocities, and were compared to SNR (Fig. 6a). The resulting plot shows SNR values were greatest for station pairs and frequencies correlating less than 2 wavelengths and decreased with increasing wavelengths. To better understand the factors controlling measurement quality, measurements were grouped into those that were either retained or discarded on the basis of unrealistic shear-wave velocities (Fig. 6a). The majority of discarded measurements were for frequencies less than ~2 Hz with separation of less than ~1.5 wavelengths. The occurrence of discarded measurements at higher wavelengths suggested that an upper wavelength limit was needed as well. New network average dispersion curves were created that discarded measurements for frequencies travelling greater than 7, 10 and 15 wavelengths. The 10 and 15 wavelength cut-offs resulted in practically no change in the dispersion curve, whereas the 7 wavelength cut-off resulted in slightly lower velocities for the two highest frequency bands and slightly greater standard deviations (Fig. S3). Enforcing an upper wavelength cut-off of 7 slightly increased the definition of shallow velocity structure (<100 m) during modelling.

To determine the minimum number of hours needed to retrieve a reliable velocity measurement, cross-correlations were stacked in 8 hr increments for the first ~2 months of the data set. SNR was found to increase steadily for the first 50 hr (Fig. 6b). After ~100 hr SNR values stabilized and stacking additional hours had little effect on the SNR of the cross-correlation. This trend was consistent for all frequency bands and station pairs. The minimum number of hours needed to reach a stable waveform and velocity estimate was found through visual assessment of cross-correlated signals with increasing number of hours for all station pairs and frequencies. No apparent trend with interstation distance was observed. A relationship with frequency can be seen for a majority of station pairs. On average, lower frequencies required more hours for the cross-correlation to converge than higher frequencies (Fig. 6c).

Over 900 hr were stacked to create the final cross-correlations for each station pair. Measurements from all station pairs were averaged at each frequency band to create a network average dispersion curve for use in the 1-D shear-wave velocity modelling. The group velocity depth sensitivity kernels provided an idea of the general range of sensitivity for these frequencies (Fig. S4). Generally, the highest sensitivity was between 20 and ~300 m depth, although the lowest frequency bands (≤2 Hz) retain some sensitivity down to 600 m. There was some degree of variability between all station pairs. This variability may be the result of differences in correlation quality due to noise and scattering, or represent true heterogeneity within the study site, or some combination of both.

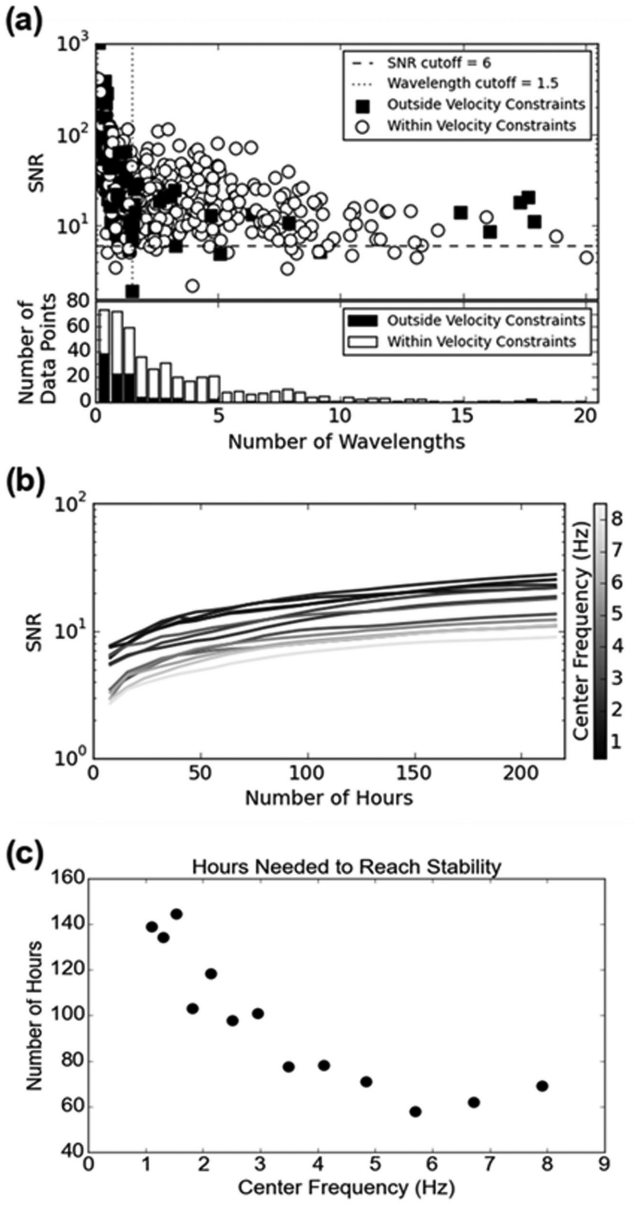

Figure 6. (a) The signal-to-noise ratio (SNR) of all the measured correlations are plotted on a semi-log scale in comparison to number of wavelengths travelled. The majority of measured velocities that were outside the accepted velocity range of 0.1–3 km (black squares) occur for wavelengths fewer than the lower cut-off criterion of 1.5. (b) SNR is shown in relation to the number of hours stacked. The average of all station pairs are shown for each frequency band. (c) The average number of hours needed for the cross-correlation to stabilize was averaged for all station pairs at each frequency band. An inverse relationship with frequency is observed.

4.2 1-D shear-wave velocity models, non-transdimensional

The non-transdimensional MCMC algorithm resulted in a family of 1000 models with the lowest error compared to the observed dispersion curve. Modelling results and consistency were strongly dependent on the number of model layers and total depth. When models were restricted to three layers and 200 m maximum depth, a high velocity zone develops that spans from ~60 to 150 m depth (Fig. 7b). A histogram of the depth to layer interfaces for the three layer models indicates that layer boundaries in the best fit models are most common at ~70 and 120 m depth. When models were

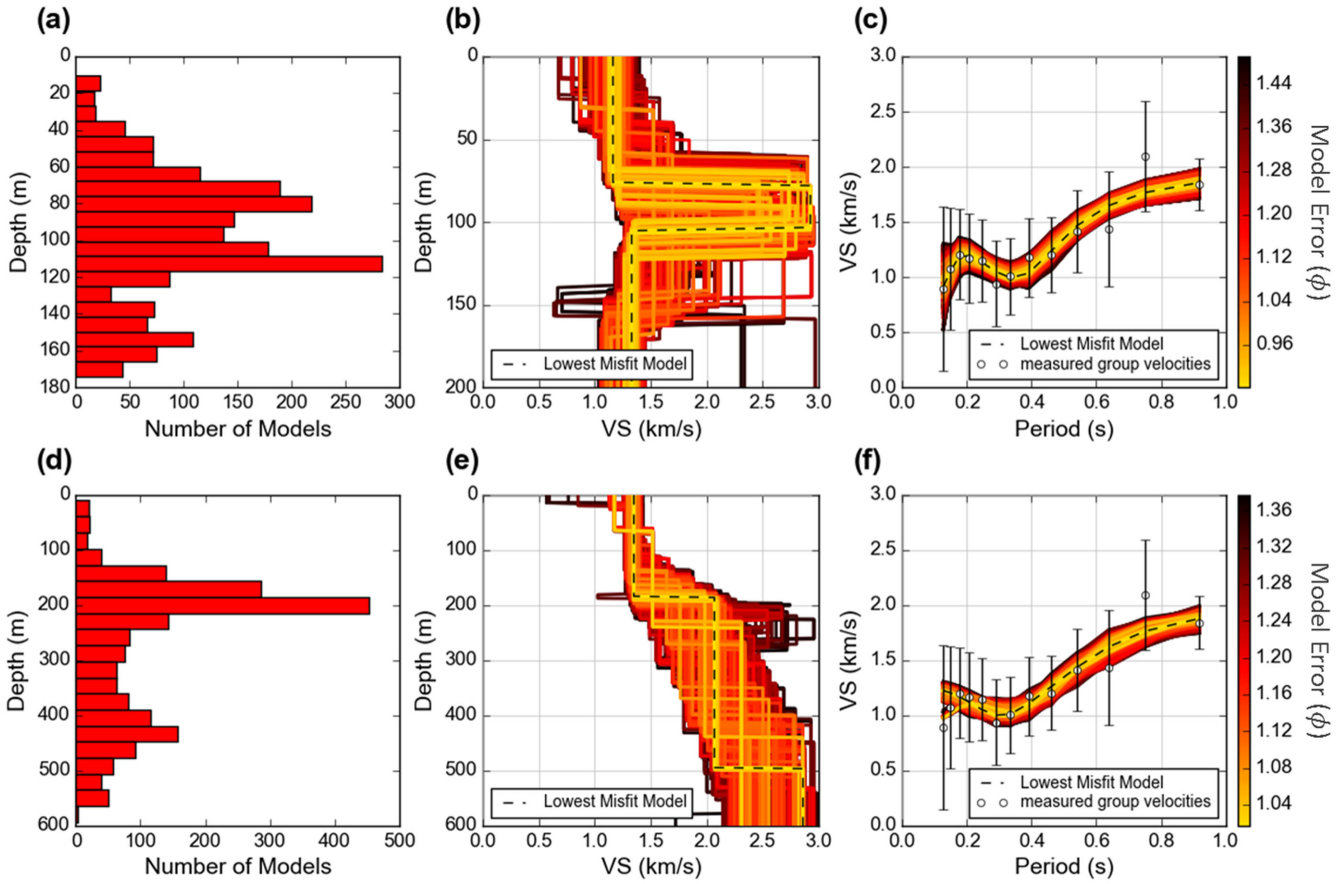

Figure 7. Results from the non-transdimensional algorithm, 3-layer models. (a) A histogram of interface depths, (b) model shear-wave velocity (V_S) profiles plotted in order of decreasing error and (c) their associated dispersion curves are shown for models constrained to a total depth of 200 m. The standard deviations for each group velocity measurement are shown as the error bars in the dispersion curve. (d)–(f) Same as (a)–(c) but for models restricted to a total depth of 600 m.

restricted to three layers, and 400 and 600 m depth, the top 200 m is most commonly modeled as a single layer and velocity, and a histogram of layer interface depths shows a dominant peak at 200 m depth (Fig. 7d). The associated dispersion curves for the deeper models fit the short period measurements poorly compared to the 200 m thickness models (Fig. 7f). Four-layered and five-layered models returned very similar results. Probability density functions for five-layered models at 200, 400 and 600 m depths showed the dependence of velocity structure on total depth (Fig. 8). A velocity increase is observed at ∼60 m depth in 200 and 400 m models but is missing in 600 m models. The shallow 200 m models suggested a discrete high velocity zone between 60 and 125 m depth, whereas 400 m models showed a step increase. Both 400 and 600 m models contained a gradational velocity increase beginning around 200 m depth and extending to about 300 m depth.

4.3 1-D shear-wave velocity models, transdimensional

The transdimensional PDFs were generally in good agreement with those from the non-transdimensional algorithm. The 400 and 600 m total depth ensembles both showed a similar gradational increase from ∼200 to ∼300 m depth. Velocity values with depth in the transdimensional PDFs were very similar to layer velocities in the non-transdimensional models, with velocities of ∼1.3 km s^{-1} above 200 m and ∼2 km s^{-1} below 200 m depth (Fig. 9). The 600 m total depth ensemble had roughly constant velocities below 400 m; therefore only the 400 m results are presented. Some discrepancies between the fixed-k and transdimensional results were, however, observed. When models were restricted to 200 m depth, the most probable structure was approximately constant velocity. The velocity increase at ∼60 m depth—resolved in the non-transdimensional models—was not apparent in the transdimensional results.

The different ensemble collection methods of the two MCMC algorithms may be the cause of the differing results. Models with constant velocities in the upper 200 m have a poorer fit to the observed data at the highest frequencies, 4–9 Hz (0.1–0.25 s). The transdimensional acceptance criterion for perturbations that change the model dimensions is balanced by the model misfit and the proposal distribution ratio (Bodin *et al*. 2012a,b). Therefore, the transdimensional algorithm can accept models with poorer fit at a higher rate than the fixed-k algorithm.

To better compare results with the non-transdimensional PDFs, the transdimensional algorithm was altered to save a separate ensemble of models with the lowest misfit, in addition to the original collection ensemble created at an even sampling rate of every *M*th model. A probability density function was then created based on the 5000 models with the lowest misfit. Velocity profiles for the 400 and 600 m total depth models are similar to the evenly sampled ensemble, though more tightly constrained. The 200 m models developed a slight curvature, with lower velocity values at the surface that gradually increased up to ∼60 m depth (Fig. 9). The 600 m models of both ensembles (lowest misfit or even sampling), tended

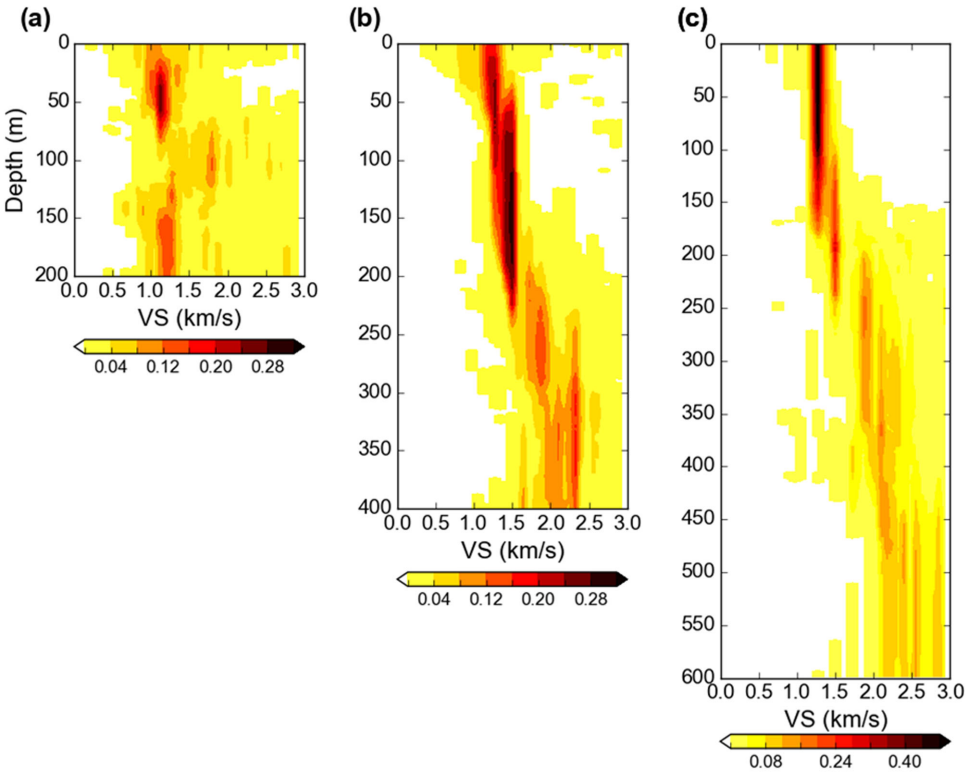

Figure 8. Probability density functions for five-layered models restricted to (a) 200 m depth, (b) 400 m depth and (c) 600 m depth. Results are very similar to the four-layered models so only the five-layered results are shown.

to select simple models with ∼4 layers (Fig. S5). The 400 m models of the lowest misfit ensemble were more commonly simpler models compared to those in the even sampling ensemble, which showed weaker preference for number of layers. The 200 m models of the lowest misfit ensemble also showed lower preference for simpler models, whereas the even sampling ensemble strongly preferred 2 layer models (Fig. S5). Both ensemble collection methods were verified using synthetic 'true' models, in which the associated dispersion curve was salted with random noise and treated as the observed data (the Appendix). Both ensembles predicted the true model velocities very well. The true interface depths were less well resolved than velocities. The minimum error ensembles more tightly constrained both the layer velocities and interface depths.

5 DISCUSSION

5.1 Data quality and deployment logistics

The application of ambient seismic noise for high frequencies (>1 Hz) entailed complications not encountered in lower frequency ambient noise studies. Group velocity measurements were unusable at low frequencies (apparent arrivals centred at zero traveltime) and difficult to pick at high frequencies due to the presence of multiple apparent arrivals. This finding precluded the use of automatic group velocity picks, reducing the expediency of the method. Difficulties in measurements were overcome by manually selecting true arrivals by tracking signals within record sections (such as in Fig. 5c), and using bounds of realistic velocities to guide arrival selection. Additionally, quality control metrics such as SNR and minimum wavelength criterion were needed in order to remove low quality data. The variability in group velocity measurements between station pairs, visible in the large standard deviations within the network average dispersion curve (Fig. 7), may reflect path dependent velocities due to true heterogeneity and/or uncertainty due to low data quality. The use of short-period seismometers instead of broad-band seismometers reduced data quality due to low gain and limited response for lower frequencies (Fig. S1). The high rejection of measurements for frequency bands below ∼2 Hz, the corner frequency of the sensors, suggests that the sensitivity of the sensors limited the low frequency end of the data set. However, this instrumentation choice was the most practical and cost effective. Another potential factor influencing data quality is the ambient noise source distribution. Fan & Snieder (2009) showed through numerical simulations that the angular distribution and density of sources strongly influences the quality of the reconstructed empirical Green's Function.

The intentionally varied interstation distances of our array configuration provided useful insights into the influence of interstation distance on cross-correlations at different frequencies. Measurements at short interstation distances and low frequencies had the highest SNR, although many such apparent signals yielded unrealistic velocities. Therefore, the number of wavelengths may be a better metric for reliable measurements than SNR. The high number of rejected measurements for short wavelengths indicates the need for a minimum wavelength retention criterion. This also suggests that the corner frequency of the sensors may not have been solely to blame for poor data quality at low (<2 Hz) frequencies. On the other hand, the drop in SNR values for increased station distances and cluster of rejected measurements beyond ∼15 wavelengths suggests that increased attenuation of high frequency waves resulted in noisier signals and larger uncertainties in velocity measurements. Thus we observe a trade-off between placing stations far enough apart to allow a sufficient number of wave cycles to propagate but not far enough to allow wave energy at these frequencies to attenuate. For this study we chose to apply an upper limit of

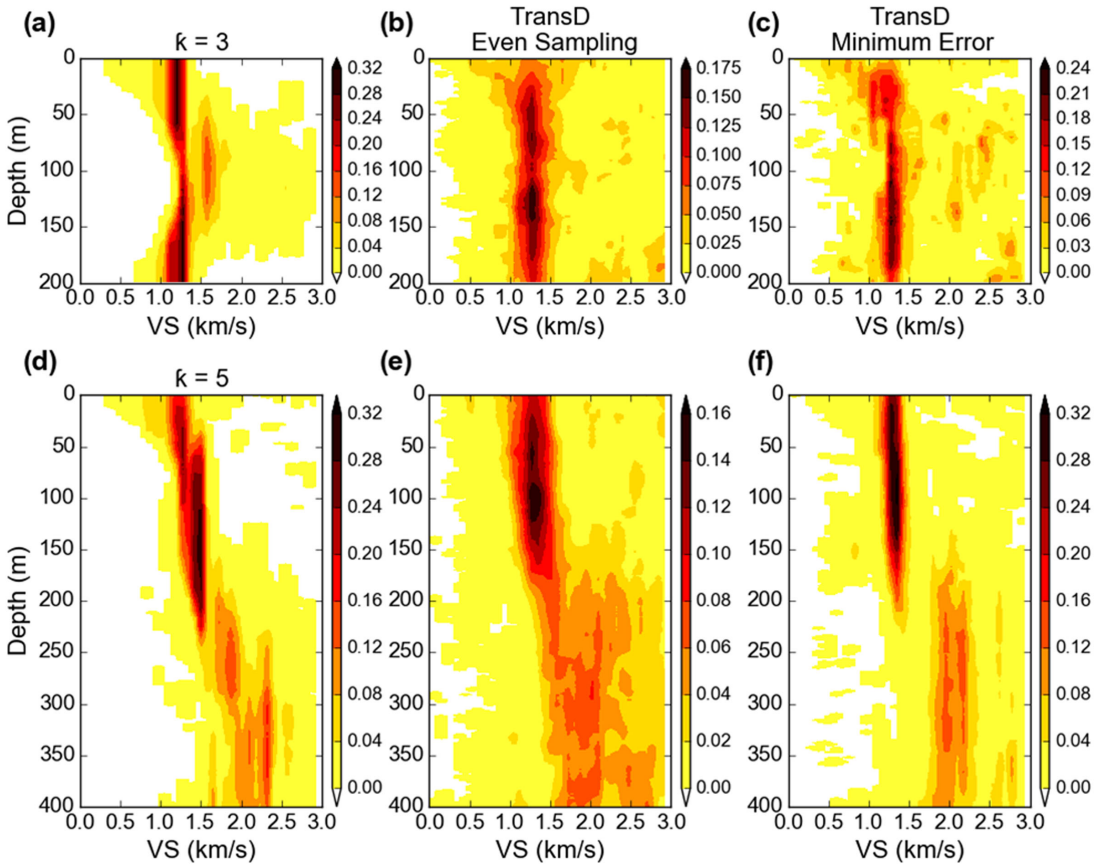

Figure 9. Comparison of probability density functions between the non-transdimensional, fixed layer models and the two collection ensembles of the transdimensional algorithm. Results for models constrained to 200 m total depth are shown for (a) the fixed 3-layer ensemble, (b) the transdimensional, even sampling ensemble, and (c) the transdimensional, minimum error ensemble. (d)–(f) Same as in (a)–(c) but for 400 m models and 5-layer non-transdimensional ensemble.

7 wavelengths which improved the constraint on shallow velocity structure (<100 m) even though it yielded slightly larger standard deviations. However, this improvement was minor and a higher limit of 15 wavelengths also produced acceptable results.

To determine if this method is practical for hydrogeological investigations, we looked at how many hours of recorded ambient seismic noise are needed in order to retrieve reliable traveltime picks. We found that the SNR of cross-correlations was maximized for all station pairs and frequencies at ~100 recorded hours. However, the time needed to reach stability of the cross-correlated waveform was found to be frequency dependent, with highest frequencies (>5 Hz) needing as little as 50 hr and the lowest frequencies (<2 Hz) requiring up to 250 hr to converge. On average, 150 hr was needed for the lowest frequency waveforms to become stable. This minimum threshold suggests at least 6.25 d of ambient noise should be recorded in order to obtain reliable group velocity measurements for network scales and diffusive wave frequencies as in our study. The limitation of only using nighttime hours in our data set increased this threshold to 18.75 d. Nonetheless, our findings suggest that ambient seismic noise can provide valuable data on submonth time frames.

5.2 1-D shear-wave velocity modelling

The results of the non-transdimensional MCMC 1-D velocity profiles showed a consistent velocity increase at ~200 m depth and, less consistently, a velocity increase at ~60 m depth. Electrical resistivity logs from the M-0650 and M-0738 boreholes show high resistivity zones from ~60 to 80 m depth, ~150–220 m, and high resistivity below ~280 m depth (Fig. 3). High electrical resistivity generally corresponds to low porosity, high density zones. Therefore, these high resistivity zones likely correspond to relatively higher seismic velocity zones within the subsurface. The zone of higher velocity in the three-layer, 200 m total depth models closely matches the top depth of the shallowest high resistivity zone in Fig. 3, and the top depth and thickness of the shallowest semi-confining unit in Fig. 2. The strong velocity increase at 200 m depth in the 1-D models roughly corresponds to the second high resistivity package seen in the M-0650 and M-0738 borehole logs. This depth also matches the second semi-confining unit seen in Fig. 2. The difference in thickness between the first and second high resistivity intervals likely explains the dominance of the second zone in the MCMC models. The second semi-confining unit from ~200 to 270 mbgs is also the confining unit believed to divide the UFAS from the LFAS and is therefore important with regards to future groundwater development plans (Williams & Kuniansky 2015).

Results from the transdimensional algorithm highlight the large uncertainty in our vertical velocity models. However, the transdimensional algorithm has the advantage of eliminating any bias in the number of layers assigned by the user on model results and allows the level of data uncertainty to scale the model dimensions. In general, models with fewer layers occurred more frequently in the

posterior distribution (Fig. S5). The parsimony inherent in Bayesian inference, as well as the high level of uncertainty in our data set, resulted in preference for simple 2–3 layered models. This preference explains the lower likelihood of a low velocity layer above ~60 m in the 400 and 600 m deep models. Collecting an ensemble based on models with lowest misfit had the potential drawback of biasing results toward more complex models. This drawback was observed by the less dominant peak of low-κ models in the 200 m minimum error ensemble compared to the even sampling ensemble. However, the 400 m minimum error ensemble showed a strong preference for simpler models, more so than the even sampling ensemble. Overall, PDFs showed a gradational velocity increase below ~150 m depth. This is consistent with the known geology of the area in that the degree of dolomitization and occurrence of evaporite deposits increase with depth in the FAS. Also, the vertical resolution of our data set decreases with depth. The effect of this can be seen in both MCMC approaches as widening of the probability density function with depth. A different array design or sensor type may have improved the resolution of the inversion; however, the results from this experiment still allowed us to identify meaningful structure.

The approach of this study was to use Bayesian inference to recover vertical velocity structure using few prior constraints, and then to compare and to validate results with known information. This was intended to evaluate and to demonstrate the utility of ambient seismic noise in areas where borehole information is limited. With little *a priori* information, modelling results agreed generally well with the known stratigraphy of the area. However, some prior constraints could have been added using information on hydrostratigraphic layers and their depths, supported by electrical resistivity logs. In addition, the resulting PDFs (both transdimensional and non-transdimensional) provide non-unique solutions. To address these issues, we conducted a final round of modelling that used previous results and additional *a priori* constraints to generate a final preferred solution. The hydrostratigraphy of the region (Fig. 2) and resistivity logs from the site (Fig. 3) suggest a discrete zone of high velocity should exist at shallow depths (<150 m). This was supported by the 200 m models, but largely missing from deeper models, which had poorer fit to the short period measurements (Fig. 7f). To resolve the discrepancy between the 200 and 400 m models, we generated fixed 5-layer models for a total depth of 400 m, but required the upper two interfaces to occur above 150 m and the second layer to have a greater velocity than adjacent layers. The final PDF, created from the 1000 models with lowest weighted misfit to the data, showed a velocity increase around 60 m depth followed by a slight decrease and then secondary increase in velocity below 200 m depth (Fig. 10a). We calculated the mean of this PDF, that is, most probable velocity with depth, to create a single, final, shear-wave velocity profile along with its 2σ confidence bounds (Fig. 10b). This velocity profile best represents the features seen in the other modelling results, and demonstrates the improvement that can be gained by forcing tighter prior constraints, when possible.

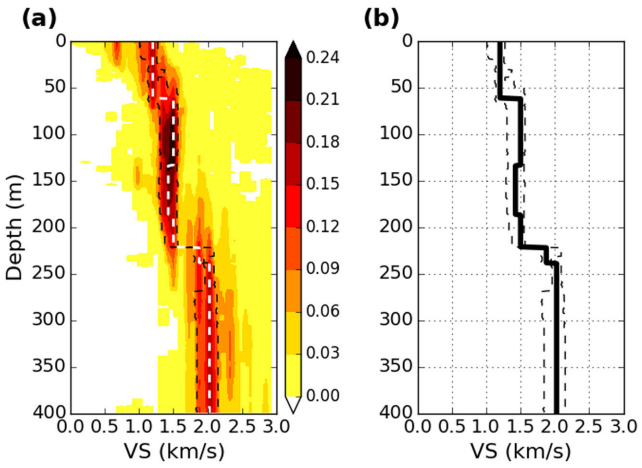

Figure 10. Final preferred model based on previous results and added constraints. (a) Probability density function and its mean (white dashed line) taken as the final velocity model for the study site (b). Both subplots show the 2σ confidence bounds (dashed black lines) around the mean velocity model.

6 CONCLUSIONS

Overall, results from the correlation of ambient noise at high (>1 Hz) frequencies show that coherent signals can be acquired and used in estimation of group velocities. However, difficulties were encountered at both low (<2 Hz) and high (>5 Hz) frequencies. The interstation distance was found to be a strong control of cross-correlation quality through its influence on the number of wavelengths travelled between pairs of stations. For this study, the range of 1.5–7 wavelengths was found to result in the most trustworthy group velocity measurements and produce the most well-defined seismic velocity structure during modelling. In addition, at least 150 hr was needed to maximize the SNR and retrieve a stable cross-correlation.

Measurements from all station pairs were combined to generate a network average dispersion curve for use in a Bayesian inference scheme employing MCMC iteration. The goal of the MCMC inversion was to retrieve an ensemble of models for interpretation of 1-D vertical velocity structure. Results from a fixed-layer approach showed increases in seismic velocity at depths that are in good agreement with the hydrostratigraphy of central Florida. The 60–125 m depth range of the shallowest confining unit was most clearly predicted by 3–5 layer models restricted to above 200 m depth. When the depth constraint was lowered, the second semi-confining unit, beginning around 200 m depth, dominated the velocity profiles. This result was observed for both fixed-layer and transdimensional approaches. The depths of high velocity zones interpreted as semi-confining units are supported by the presence of high-resistivity zones seen in boreholes at the study site. Therefore, meaningful velocity structure was observable using little *a priori* information; however, the addition of tighter prior constraints did help resolve some of the discrepancy between models of different depths.

Results show that the non-transdimensional algorithm provides a promising method for identifying high velocity zones corresponding to confining units; however, profiles are highly dependent on the number of layers. Using a transdimensional approach provided a better understanding of the ensemble uncertainty, as well as revealing the most robust features of the 1-D velocity profiles. By freeing the κ parameter, we avoid bias in the inversion results. The fixed-κ approach constructed more detailed structure, but the transdimensional approach highlights what structure can be interpreted with the greatest confidence. Therefore, we found the use of both approaches useful for this study. Even though the nonunique aspect of Bayesian inference provides important insights into data uncertainty, a preferred solution can be more helpful for interpretation and use of these results in future studies. Therefore, we used the mean

of the final PDF to represent the preferred solution for shear-wave velocity at our study site.

Modelling results of ambient seismic noise data matched a known seismic velocity increase corresponding to an important semi-confining unit of the FAS in central Florida. This suggests ambient noise could prove a valuable new investigative technique for groundwater studies. However, high levels of data uncertainty from the ambient noise cross-correlations proved a disadvantage to this technique. In this study, we identified key factors influencing cross-correlation quality (e.g. interstation distances, number of hours stacked). However, other potential factors such as sensor type or distribution and density of sources were not addressed. This leaves open possibilities for future work in testing azimuthal distributions of high-frequency (>1 Hz) ambient noise sources and potential improvements to be gained through using broad-band seismometers.

ACKNOWLEDGEMENTS

Funding from the Gulf Coast Association of Geological Societies through a student grant to Stephanie James made this project possible. We are very grateful to Noel Barstow and Pnina Miller of the IRIS-PASSCAL Instrument Center for all their instruction in the use and maintenance of the IRIS-PASSCAL seismic equipment deployed during this project. We are grateful to George Slad of the PASSCAL Instrument Center for his help with archiving the seismic data collected. We would like to thank Jeff Davis at St. Johns River Water Management District for assistance with the site selection and permitting, as well as helpful discussions. Thank you to Florida Forest Service for use of their land in this study. We would also like to thank Lanie Meridth at University of Florida for helpful discussions.

REFERENCES

Anselmetti, F.S. & Eberli, G.P., 1993. Controls on sonic velocity in carbonates, *Pure appl. Geophys.,* **141,** 287–323.

Bensen, G.D., Ritzwoller, M.H., Barmin, M.P., Levshin, A.L., Lin, F., Moschetti, M.P., Shapiro, N.M. & Yang, Y., 2007. Processing seismic ambient noise data to obtain reliable broad-band surface wave dispersion measurements, *Geophys. J. Int.,* **169,** 1239–1260.

Bensen, G.D., Ritzwoller, M.H. & Shapiro, N.M., 2008. Broadband ambient noise surface wave tomography across the United States, *J. geophys. Res.,* **113**(B5), doi:10.1029/2007JB005248.

Bodin, T. & Sambridge, M., 2009. Seismic tomography with the reversible jump algorithm, *Geophys. J. Int.,* **178,** 1411–1436.

Bodin, T., Sambridge, M., Tkalčić, H., Arroucau, P., Gallagher, K. & Rawlinson, N., 2012a. Transdimensional inversion of receiver functions and surface wave dispersion, *J. geophys. Res.,* **117,** B02301, doi:10.1029/2011JB008560.

Bodin, T., Sambridge, M., Rawlinson, N. & Arroucau, P., 2012b. Transdimensional tomography with unknown data noise, *Geophys. J. Int.,* **189,** 1536–1556.

Brenguier, F., Clarke, D., Aoki, Y., Shapiro, N.M., Campillo, M. & Ferrazzini, V., 2011. Monitoring volcanoes using seismic noisecorrelations, *Comptes Rend. Geosci.,* **343,** 633–638.

Campillo, M., 2006. Phase and correlation in 'random' seismic fields and the reconstruction of the green function, *Pure appl. Geophys.,* **163,** 475–502.

Campillo, M. & Paul, A., 2003. Long-range correlations in the diffuse seismic coda, *Science,* **299,** 547–549.

Chaves, E.J. & Schwartz, S.Y., 2016. Monitoring transient changes within overpressured regions of subduction zones using ambient seismic noise, *Sci. Adv.,* **2**(1), e1501289, doi:10.1126/sciadv.1501289.

Copeland, R., Upchurch, S.B., Scott, T.M., Kromhout, C., Arthur, J., Means, G., Rupert, F. & Bond, P., 2009. *Hydrogeologic Units of Florida*, Florida Geological Survey Special Publication 28, Tallahassee, Florida.

Fan, Y. & Snieder, R., 2009. Required source distribution for interferometry of waves and diffusive fields, *Geophys. J. Int.,* **179,** 1232–1244.

Gallego, A., Russo, R.M., Comte, M., Mocanu, V.I., Murdie, R.E. & Vandecar, J.C., 2010. Seismic Noise Tomography in the Chile ridge subduction region, *Geophys. J. Int.,* **182,** 1478–1492.

Gassenmeier, M., Sens-Schönfelder, C., Delatre, M. & Korn, M., 2015. Monitoring of environmental influences on seismic velocity at the geological storage site for CO_2 in Ketzin (Germany) with ambient seismic noise, *Geophys. J. Int.,* **200,** 524–533.

Halliday, D., Curtis, A. & Kragh, E., 2008. Seismic surface waves in a suburban environment: active and passive interferometric methods, *Leading Edge,* **2,** 210–218.

Herrmann, R.B. & Ammon, C.J., 2002. *Computer Programs in Seismology: Surface Waves, Receiver Functions, and Crustal Structure,* St. Louis University.

Kazatchenko, E., Markov, M., Mousatov, A. & Parra, J.O., 2006. Carbonate microstructure determination by inversion of acoustic and electrical data: application to a south Florida aquifer, *J. appl. Geophys.,* **59,** 1–15.

Lawrence, J.F., Denolle, M., Seats, K.J. & Prieto, G.A., 2013. A numeric evaluation of attenuation from ambient noise correlation functions, *J. geophys. Res.,* **118,** 6134–6145.

Lin, F.-C., Li, D., Clayton, R.W. & Hollis, D., 2013. High-resolution 3D shallow crustal structure in Long Beach, California: application of ambient noise tomography on a dense seismic array, *Geophysics,* **78,** Q45–Q56.

Lin, F.-C., Moschetti, M.P. & Ritzwoller, M.H., 2008. Surface wave tomography of the western United States from ambient seismic noise: Rayleigh and Love wave phase velocity maps, *Geophys. J. Int.,* **173,** 281–298.

Lobkis, O.I. & Weaver, R., 2001. On the emergence of the Green's function in the correlations of a diffuse field, *J. acoust. Soc. Am.,* **110,** 3011–3017.

Mainsant, G., Larose, E., Bronnimann, C., Jongmans, D., Michoud, C. & Jaboyedoff, M., 2012. Ambient seismic noise monitoring of a clay landslide: toward failure prediction, *J. geophys. Res.,* **117,** F01030, doi:10.1029/2011JF002159.

Malinverno, A., 2002. Parsimonious Bayesian Markov chain Monte Carlo Inversion in a nonlinear geophysical problem, *Geophys. J. Int.,* **151,** 675–688.

Maliva, R.G. & Walker, C.W., 1998. Hydrogeology of deep-well disposal of liquid wastes in southwestern Florida, USA, *Hydrogeol. J.,* **6,** 538–548.

Miller, J.A., 1986. Hydrogeologic framework of the Floridan aquifer system in Florida and in parts of Georgia, Alabama, and South Carolina, in U.S. Geological Survey Professional Paper, Regional Aquifer-System Analysis Program 1403-B.

Mordret, A., Landes, M., Shapiro, N.M., Singh, S.C., Roux, P. & Barkved, O.I., 2013. Near-surface study at the Valhall oil field from ambient noise surface wave tomography, *Geophys. J. Int.,* **193,** 1627–1643.

Moschetti, M.P., Ritzwoller, M.H. & Shapiro, N.M., 2007. Surface wave tomography of the western United States from ambient seismic noise: Rayleigh wave group velocity maps, *Geochem. Geophys. Geosyst.,* **8,** Q08010, doi:10.1029/2007GC001655.

MWH Americas, Inc., 2004. North Lee County water treatment plant: Class I injection well and dual zone monitoring well. Drilling and Testing Report.

Ojo, A.O., Ni, S. & Li, Z., 2017. Crustal radial anisotropy beneath Cameroon from ambient noise tomography, *Tectonophysics,* **696,** 37–51.

Pan, Y., Xia, J., Xu, Y., Xu, Z., Cheng, F., Xu, H. & Gao, L., 2016. Delineating shallow *S*-wave velocity structure using multiple ambient-noise surface-wave methods: an example from Western Junggar, China, *Bull. seism. Soc. Am.,* **106**(2), 327–336.

Parra, J.O., Hackert, C.L. & Bennett, M.W., 2006. Permeability and porosity images based on *P*-wave surface seismic data: application to a south Florida aquifer, *Water Resour. Res.,* **42,** W02415, doi:10.1029/2005WR004114.

Parra, J.O., Hackert, C.L., Richardson, E. & Clayton, N., 2009. Porosity and permeability images based on crosswell seismic measurements integrated

with FMI logs at the Port Mayaca aquifer, South Florida, *Leading Edge,* **10,** 1212–1219.
Picozzi, M., Parolai, S., Bindi, D. & Strollo, A., 2009. Characterization of shallow geology by high-frequency seismic noise tomography, *Geophys. J. Int.,* **176,** 164–174.
Roux, P., Sabra, K.G., Kuperman, W.A. & Roux, A., 2005. Ambient noise cross correlation in free space: theoretical approach, *J. acoust. Soc. Am,* **117,** 79–84.
Sabra, K.G., Gerstoft, P., Roux, P., Kuperman, W.A. & Fehler, M.C., 2005. Extracting time-domain Green's function estimates from ambient seismic noise, *Geophys. Res. Lett.,* **32,** L03310, doi:10.1029/2004GL021862.
Sens-Schönfelder, C. & Wegler, U., 2006. Passive image interferometry and seasonal variations of seismic velocities at Merapi Volcano, Indonesia, *Geophys. Res. Lett.,* **33,** L21302, doi:10.1029/2006GL027797.
Shapiro, N.M. & Campillo, M., 2004. Emergence of broadband Rayleigh waves from correlations of the ambient seismic noise, *Geophys. Res. Lett.,* **31,** 1–4.
Shapiro, N.M., Campillo, M., Stehly, L. & Ritzwoller, M.H., 2005. High-resolution surface-wave tomography from ambient seismic noise, *Science,* **307,** 1615–1618.
Shirzad, T., Shomali, Z.H., Naghavi, M. & Norouzi, R., 2015. Near-surface vs Structure by inversion of surface wave estimated from ambient seismic noise, *Near Surf. Geophys.,* **13,** doi:10.3997/1873-0604.2015031.
St. Johns River Water Management District, M-0650, Hydrogeologic information system. Available at: http://publicserver1.sjrwmd.com/vlpub/vlwebpub/, last accessed 1 November 2014.
Tibbals, C.H., 1990. Hydrology of the Floridan aquifer system in East-Central Florida, in U.S. Geological Survey Professional Paper, 1403–E.
Tsai, V.C., 2009. On establishing the accuracy of noise tomography travel-time measurements in a realistic medium, *Geophys. J. Int.,* **178,** 1555–1564.
Williams, L.J. & Kuniansky, E.L., 2015. Revised hydrogeologic framework of the Floridan aquifer system in Florida and Parts of Georgia, Alabama, and South Carolina, in U.S. Geological Survey Professional Paper 1807.
Yang, Y., Ritzwoller, M.H., Levshin, A.L. & Shapiro, N.M., 2007. Ambient noise Rayleigh wave tomography across Europe, *Geophys. J. Int.,* **168,** 259–274.
Yao, H., van der Hilst, R.D. & de Hoop, M., 2006. Surface-wave array tomography in SE Tibet from ambient seismic noise and two-sation analysis – I. Phase velocity maps, *Geophys. J. Int.,* **166,** 732–744.
Zhang, J., Gerstoft, P. & Shearer, P.M., 2009. High-frequency *P*-wave seismic noise driven by ocean waves, *Geophys. Res. Lett.,* **36,** L09302, doi:10.1029/2009GL037761.

SUPPORTING INFORMATION

Supplementary data are available at *GJIRAS* online.

Figure S1. Instrument response curves are shown for the L22 short-period geophone used in this study as well as a common broad-band sensor (STS2). The L22 geophone has a corner frequency of 2 Hz. Frequencies less than 2 Hz require increasingly more energy to produce the same response as frequencies greater than 2 Hz ('Sensor Comparison Chart', IRIS PASSCAL).
Figure S2. The signal-to-noise ratio (SNR) of all the measured correlations are plotted on a semi-log scale in comparison to the (a) interstation distances, (b) frequency and (c) wavelength, assuming a velocity of 1 km s^{-1}.
Figure S3. Comparison of network average dispersion curves with no upper wavelength limit (black) and an upper limit of 7 wavelengths (red).
Figure S4. (a) Representative shear-wave velocity model, based on inversion results, and the associated (b) group velocity depth sensitivity kernels for the 13 frequency bands used in this study. The range of ~20–300 m has the highest sensitivities. Vertical resolution decreases with depth.
Figure S5. Histograms are shown for the number of layers, k, in posterior distribution of models from the transdimensional MCMC algorithm. (a)–(c) Results from the evenly sampled ensemble for the 200, 400 and 600 m depth constraints, respectively. (d)–(f) Results from the minimum-error ensemble for the 200, 400 and 600 m depth constraints, respectively.
Table S1. Values of parameters defined in MCMC algorithm.

Please note: Oxford University Press is not responsible for the content or functionality of any supporting materials supplied by the authors. Any queries (other than missing material) should be directed to the corresponding author for the paper.

APPENDIX: VERIFICATION TESTS

A series of verification tests were completed to test the accuracy and resolution of the transdimensional modelling results. True models were constructed and used to generate synthetic dispersion curves using *surf96* (Herrmann & Ammon 2002). Random noise was added to each measurement in the dispersion curve to create the synthetic observed data ($\mathbf{d}_{obs}$). The noise values added were also used as the standard deviations ($\boldsymbol{\sigma}_{\mathbf{d}}$) for weighting in the inversion. The transdimensional algorithm was then executed with the same parameters as before. Two final model ensembles are created: the first from evenly sampling every Mth model of the posterior distribution, the second from retaining the 5000 models from the posterior distribution with the lowest weighted misfit, $\phi(\mathbf{m})$.

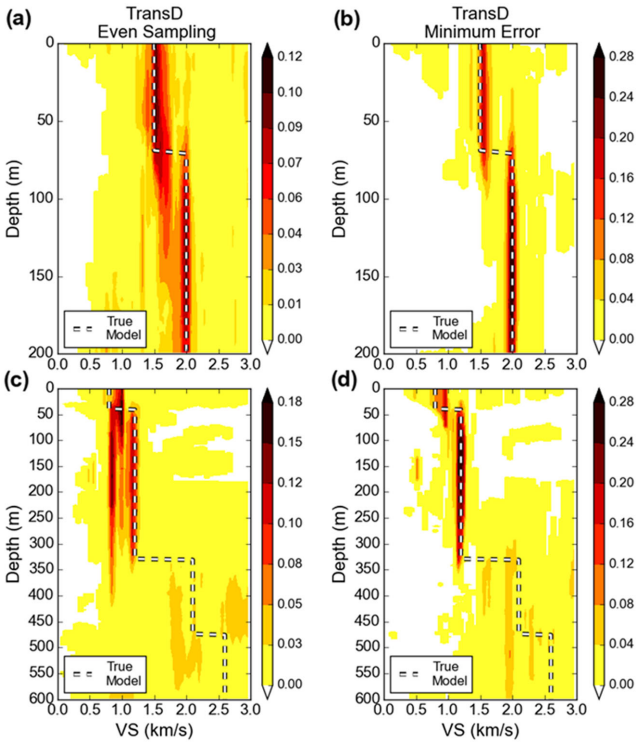

Figure A1. Probability density functions for verification test results of the transdimensional algorithm. The true models are shown by the dashed lines. Results for the 200 m models are shown for the (a) even sampling ensemble, and (b) the minimum error ensemble. (c)–(d) Same as in (a)–(b) but for the 600 m models.

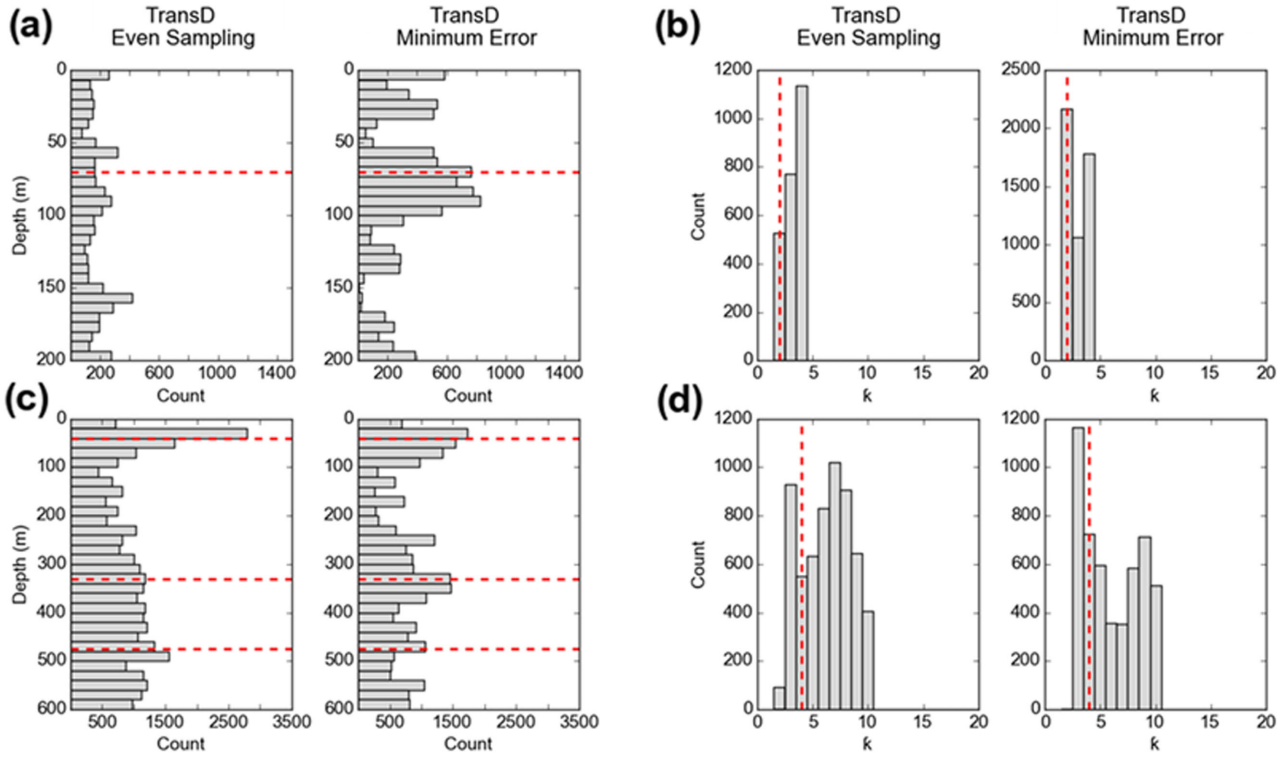

Figure A2. Verification test results of the transdimensional algorithm. (a) Histograms of interface depths for both final ensembles of the 200 m models. Interface depths of the true models are shown with dashed red lines. (b) Histograms of the number of layers for both final ensembles of the 200 m models. Number of layers in the true models are shown with dashed red lines. (c)–(d) Same as in (a)–(b) but for the 600 m models.

A variety of true models were tested. The probability density functions (PDFs) for two runs, 200 and 600 m depth constraints, are shown in Fig. A1. The layer velocities were very well matched for both runs, however the minimum error ensemble more tightly resolved the layer velocities. The 600 m results show that layer velocities below ∼350 m depth were poorly recovered. Interface depths were also well matched, overall. The even sampling ensemble for 200 m models show a large range in uncertainty of the interface depth (Fig. A1a). This is also seen in the histogram of interface depths (Fig. A2a). By retaining models best fit to the observed data, the range of uncertainty surrounding the true interface at 70 m depth is reduced (Figs A1b and A2a). Similarly, the PDFs for the 600 m models show a better prediction of the shallow 40 m interface in the minimum error ensemble. However, the histogram of interface depths reveal that the 40 m interface is well predicted in both ensembles (Fig. A2c). The 330 m interface is observed in both ensemble PDFs, however the interface histograms show that the minimum error ensemble contains a higher likelihood for this interface. Neither ensemble recovered the 475 m interface. Both ensembles of the 200 m models show a preference for simple models (Fig. A2b). The deeper, 600 m, models have a higher likelihood for more complicated models, that is, more layers (Fig. A2d). For both depth constraints, the minimum error ensembles better predict the true number of layers.

Verification test results show that the transdimensional algorithm is best able to recover layer velocities. Interface depths contain more uncertainty but are generally well resolved. The lower range of depth sensitivity can be observed in the poor recover of layer velocities and interfaces below ∼350 m depth. Test results also highlight the differences between the two ensemble collection methods. The minimum error ensemble returns the best prediction of the true models. However, the even sampling ensemble provides valuable insights into the range of models within the posterior distribution and therefore an assessment of the uncertainty in the modelling results.